

Representative-volume sizing in finite cylindrical computed tomography by low-wavenumber spectral convergence

Fernando Alonso-Marroquin,^{1,*} Abdullah Alqubalee,¹ and Christian Tantardini^{1,†}

¹Center for Integrative Petroleum Research, King Fahd University of Petroleum and Minerals, Dhahran 31261, Saudi Arabia

(Dated: January 15, 2026)

Choosing a representative element volume (REV) from finite cylindrical μ CT scans becomes ambiguous when a key field variable exhibits a slow axial trend, because estimated statistics can change systematically with subvolume size and position rather than converging under simple averaging. A practical workflow is presented to size an REV under such nonstationary conditions by first suppressing axial drift/trend to obtain a residual field suitable for second-order analysis, and then selecting the smallest analysis diameter for which low-wavenumber content stabilizes within a prescribed tolerance. The approach is demonstrated on *Thalassinoides*-bearing rocks, whose branching, connected burrow networks impose heterogeneity on length scales comparable to typical laboratory core diameters, making imaging-based microstructural statistics and downstream digital-rock proxies highly sensitive to the chosen subvolume. From segmented data, a scalar “burrowsity” field—capturing burrow-related pore spaces and infills—is defined, and axial detrending (with optional normalization) is applied to mitigate acquisition drift and nonstationary trends. Representativeness is then posed as a diameter-convergence problem on nested inscribed cylinders: the two-point covariance and its isotropic spectral counterpart \hat{C} are estimated, and the smallest diameter at which the low-wavenumber plateau becomes stable is selected. Applied to a segmented *Thalassinoides* core, the method identifies a minimum analysis cylinder of approximately $D_{\text{REV}} \approx 93$ mm and $H_{\text{REV}} \approx 83$ mm, enabling reproducible correlation-scale reporting and connectivity-sensitive property estimation.

I. INTRODUCTION

Branching three-dimensional (3D) burrow systems assigned to the ichnogenus *Thalassinoides* are widely recognized as characteristic expressions of macroscale bioturbation in shallow-marine sedimentary rocks [1–3]. Its architecture is typically organized as interconnected tunnel networks with frequent T- and Y-junctions, locally forming boxworks or maze-like geometries; depending on depositional conditions and diagenetic overprint [4, 5]. These structures may be preserved as open pore spaces, as sediment-filled casts, or as cemented infills [4, 5], collectively referred to here as *burrowosity*. In core-scale specimens, a “mottled” texture is often reported, in which a comparatively fine-grained host matrix is overprinted by a geometrically complex burrow phase whose characteristic length scales span from the tube diameter (millimeters) to network connectivity across centimeters [4].

From a petrophysical and geomechanical standpoint, this fabric is not a visual curiosity. Because the burrow phase is frequently better connected than the surrounding pore space, preferential flow pathways, directional contrasts, and strong scale effects in measured transport properties can be induced in *Thalassinoides*-bearing ichnofabrics. This behavior has been increasingly documented in reservoir-oriented studies of burrowed media, where a small number of connected junctions or dominant tunnels can control effective connectivity and per-

meability upscaling behavior at the plug-to-core transition [6, 7].

Direct 3D imaging of such fabrics is enabled by medical computed tomography (CT), and quantitative “digital rock” analysis is thereby facilitated. In contemporary workflows, porosity statistics, connectivity measures, correlation descriptors, and simulation-ready subdomains for flow or elastic calculations are routinely extracted [8, 9]. A specific difficulty is, however, encountered in burrowed rocks: the dominant heterogeneity length associated with the burrow network can be comparable to the scanned core diameter. In that regime, property estimates are not merely noisy at small volumes; systematic bias can be introduced by insufficient sampling of low-wavenumber structure (large-scale connectivity), and by whether a subvolume includes or excludes a small number of key junctions.

Accordingly, the selection of a *representative volume* is brought to the foreground. For a finite cylindrical CT scan, the smallest cylinder diameter (and corresponding axial extent) is sought such that estimated statistics of a chosen field (e.g., a burrow/host indicator or a burrowsity proxy) become insensitive, within tolerance, to further increases in sampled volume. In the porous-media literature, this threshold is commonly referred to as the *representative elementary volume* (REV) [10], while closely related usage in heterogeneous solids and composites often employs the term *representative volume element* (RVE) [11, 12]. Operationally, representativeness is assessed through finite-size convergence: low-order descriptors (means and variances, and—once near-stationarity is enforced—two-point statistics such as covariance or spectrum) are expected to stabilize as

* fernando.marroquin@kfupm.edu.sa

† christiantantardini@ymail.com

the window size is increased [13]. In tomography-based porous media, this principle is commonly implemented by evaluating nested subvolumes matched to the acquisition geometry, including cylindrical windows for core scans [14]. For *Thalassinoides*-bearing samples, two issues become central: (i) a finite cylinder rather than a periodic box is imposed by the imaging support, and (ii) pronounced nonstationarity can be present due to acquisition artifacts and geological trends, which must be mitigated before covariance- or spectrum-based diagnostics are meaningful [15].

A useful organization of the problem is obtained by treating REV sizing as a finite-size convergence question controlled by the low-wavenumber content of the microstructure: when long-wavelength structure is not adequately sampled, any estimator of correlation scale (and downstream effective properties) remains diameter-dependent. This perspective is consistent with the recent covariance/spectrum-driven sizing analysis of finite computational domains in stationary random media [16]. Here, the same logic is adapted to a connectivity-dominated geological fabric imaged as a segmented CT cylinder, for which (a) a preprocessing route yielding a near-stationary fluctuation field and (b) a diameter-focused convergence criterion formulated on nested cylinders are required.

Concretely, the workflow is composed of two components.

a. Preprocessing to obtain a near-stationary “burrowsity” field. Starting from a masked and segmented cylindrical volume, a scalar field is defined to encode the presence of *Thalassinoides*-related structure (e.g., a Boolean burrow/host indicator or a derived proxy). Slow trends (axial drift, beam hardening, and other low-frequency components) are then removed and fluctuations are retained that are approximately weakly stationary over the analysis window, so that second-order statistics can be interpreted.

b. A \hat{C} -test for selecting an optimal cylinder diameter. On nested cylinders of increasing diameter, the two-point covariance (and its Fourier/Hankel counterpart \hat{C}) of the detrended field is estimated and the stability of low-wavenumber descriptors is monitored. The diameter is deemed representative once these descriptors converge within tolerance, indicating that sufficient long-wavelength connectivity information has been captured and that further enlargement does not materially change inferred correlation scales.

Overall, a covariance/spectrum-based convergence philosophy is operationalized for REV sizing in burrowed rocks, while the two practical features that dominate CT applications—nonstationarity and finite cylindrical support—are explicitly accounted for.

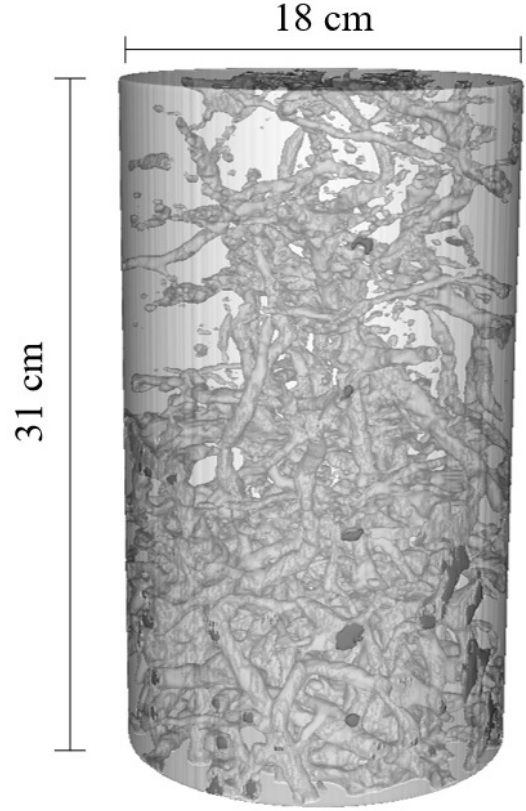


FIG. 1. Core sample of *Thalassinoides* rock used in the analysis. The analyzed CT dataset corresponds to a segmented cylindrical core with dimensions $488 \times 488 \times 160$ voxels (transverse size $N_x = N_y = 488$ pixels and axial length $N_z = 160$ slices). The physical specimen dimensions were $D_s = 180$ mm in diameter and $H_s = 310$ mm in height, implying voxel spacings $\Delta x = \Delta y = D_s/488 \simeq 0.369$ mm/pixel and $\Delta z = H_s/160 \simeq 1.94$ mm/slice.

II. DETRENDING AND DENOISING OF “BURROWSITY”

In covariance- or spectrum-based REV criteria, it is implicitly assumed that the analyzed field is (at least) *weakly stationary* over the window of interest: the mean is approximately constant and second-order statistics depend primarily on spatial separation rather than absolute position. In practice, this assumption is rarely satisfied by raw μ CT data of geological samples without preprocessing. Long-wavelength intensity drift, beam hardening, ring artifacts, and genuine geological gradients can introduce low-frequency components that dominate the estimated covariance at large lags, thereby inflating inferred correlation lengths and, consequently, the REV size. Beam-hardening artifacts are a classical source of such bias in CT, producing cupping and spatially varying attenuation unrelated to microstructure [17, 18]; ring artifacts introduce spurious concentric structures that con-

taminate radial statistics [19]. In the present section, an operational “burrowsity” field is defined and a detrending/denoising pipeline is specified so that a fluctuation field suitable for second-order convergence tests is obtained.

A. Burrowsity field and detrending to enforce weak stationarity

The diameter-selection criterion developed in Sec. III is formulated in terms of second-order statistics (covariance and its spectral counterpart), and a scalar field is therefore required whose fluctuations can be interpreted as real microstructural variability rather than acquisition drift. In a *Thalassinoides*-bearing specimen, the most robust choice for this purpose is a phase-indicator-type field that tracks the burrow-related phase (burrow void, cast, or cemented infill depending on the segmentation target) on the masked cylindrical support.

Let $I_{\text{raw}}(\mathbf{x})$ denote the reconstructed grayscale μCT volume, with voxel-center coordinate $\mathbf{x} = (x, y, z)$. Let $M(\mathbf{x}) \in \{0, 1\}$ be the cylindrical mask (one inside the core, zero outside), and let the masked intensity be defined as

$$I(\mathbf{x}) = M(\mathbf{x}) I_{\text{raw}}(\mathbf{x}), \quad \mathbf{x} \in \Omega_{\text{box}}, \quad (1)$$

so that the effective analysis domain is $\Omega_{\text{cyl}} = \{\mathbf{x} : M(\mathbf{x}) = 1\}$. In the simplest and most reproducible implementation for REV sizing, *burrowsity* is defined as the Boolean indicator obtained by thresholding I ,

$$B(\mathbf{x}) = \begin{cases} 1, & I(\mathbf{x}) \geq T, \\ 0, & I(\mathbf{x}) < T, \end{cases} \quad \mathbf{x} \in \Omega_{\text{cyl}}, \quad (2)$$

where T is a chosen threshold. In practice, T may be selected manually to match geological interpretation and training slices, or it may be determined by an objective grayscale criterion such as Otsu’s method for bimodal histograms [20], with the caveat (well known in porous-media microtomography) that partial-volume effects, phase overlap in attenuation, and reconstruction artifacts can render histogram-only criteria insufficient without domain knowledge [15, 21]. For REV sizing, Eq. (2) is intentionally minimal: it is required primarily that the field be computed *consistently* across nested cylinders so that observed diameter-dependence can be attributed to sampling and not to changing preprocessing.

A convenient decomposition is obtained by separating mean phase fraction from fluctuations. For any analysis domain $\Omega \subseteq \Omega_{\text{cyl}}$,

$$\bar{B}_\Omega = \frac{1}{|\Omega|} \sum_{\mathbf{x} \in \Omega} B(\mathbf{x}), \quad \delta B(\mathbf{x}) = B(\mathbf{x}) - \bar{B}_\Omega. \quad (3)$$

The subsequent steps are designed so that δB is not dominated by slow drift (nonstationary mean) or by structured artifacts that would otherwise leak into the low-wavenumber part of the covariance/spectrum.

In burrowed rocks, long-wavelength structure may be geological (layering, cementation gradients, preferential burrow orientation), but in μCT data it may also be produced by acquisition and reconstruction artifacts. This distinction is critical because the \widehat{C} -test is driven precisely by *low* wavenumbers: any spurious drift or structured artifact injects artificial long-range correlations and biases the inferred diameter upward.

Three effects are particularly relevant.

(i) *Beam hardening and cupping.* In polychromatic CT, preferential attenuation of low-energy photons produces an effective hardening of the beam with path length. In reconstructed volumes this commonly appears as a radial intensity gradient (cupping) and other position-dependent biases [17, 18]. For natural materials with strong heterogeneity, dedicated beam-hardening correction procedures are often required to avoid bias in quantitative descriptors [22].

(ii) *Ring artifacts.* Detector nonuniformities and reconstruction imperfections can generate concentric rings in slices. Because the statistics used here are radial/cylindrical by design, ring artifacts are especially pernicious: an artificial radial signature is introduced that can be misread as genuine long correlation length [19]. Ring-artifact reduction is therefore not merely cosmetic; it is a prerequisite when the analysis itself is radial.

(iii) *Slice-to-slice drift and other low-frequency trends.* Scanner instabilities, reconstruction regularization, and/or genuine geological trends can generate slow axial drift in the mean intensity and, after segmentation, in the segmented phase fraction. This issue is widely discussed in pore-scale imaging workflows because it couples field-of-view, grayscale variability, and apparent representativeness [23, 24]. If uncorrected, the empirical covariance of a finite cylinder can exhibit slow decay or apparent plateaus that do not reflect microstructure.

To isolate microstructural fluctuations from slow axial drift, the analysis is begun with the slice-wise phase-fraction signal

$$\phi(z_k) = \langle B(x, y, z_k) \rangle_{x, y} = \frac{1}{|\Omega_{xy}(z_k)|} \sum_{(x, y) \in \Omega_{xy}(z_k)} B(x, y, z_k), \quad (4)$$

where $\Omega_{xy}(z_k) = \{(x, y) : M(x, y, z_k) = 1\}$ is the in-slice support. A smooth trend $\mu_w(z_k)$ is then constructed by a moving-average (rolling-mean) filter of width w slices,

$$\mu_w(z_k) = \frac{1}{w} \sum_{j=k-\lfloor w/2 \rfloor}^{k+\lfloor w/2 \rfloor} \phi(z_j), \quad (5)$$

with endpoint handling implemented by truncation or reflection in practice. The detrended field is defined by subtracting the axial trend *slice-wise*,

$$b(\mathbf{x}) = B(\mathbf{x}) - \mu_w(z), \quad \mathbf{x} \in \Omega_{\text{cyl}}, \quad (6)$$

so that (approximately) zero mean across z is enforced while the burrow-network geometry in (x, y) is preserved.

When the variance is also observed to drift with z (e.g., due to changing contrast or layering), an additional slice-wise standardization can be applied,

$$\tilde{b}(\mathbf{x}) = \frac{B(\mathbf{x}) - \mu_w(z)}{\sigma_w(z) + \varepsilon}, \quad (7)$$

$$\sigma_w^2(z_k) = \left\langle (B - \mu_w(z_k))^2 \right\rangle_{x,y}, \quad (8)$$

where ε prevents numerical issues in near-constant slices. This normalization is intended to target *weak stationarity* over the analysis window: a nearly constant mean and a covariance that depends primarily on separation, not on absolute position. Since the downstream criteria are second-order, this is the relevant notion of stationarity for the \widehat{C} -based diameter test [25].

Finally, the choice of the window size w is required to be large enough to remove slow drift but not so large that genuine burrow-scale intermittency is suppressed. A compact diagnostic is provided by the excess kurtosis of the detrended axial signal $r(z_k) = \phi(z_k) - \mu_w(z_k)$,

$$K_{\text{ex}}(w) = \frac{m_4}{m_2^2} - 3, \quad (9)$$

$$m_p = \frac{1}{M} \sum_{k=1}^M (r(z_k) - \bar{r})^p, \quad (10)$$

which tracks deviations from Gaussian-like residual fluctuations as w is varied [25]. In Sec. II, this criterion is used, together with covariance/spectrum consistency checks, to select a window width that yields a residual field suitable for the subsequent \widehat{C} -test on nested cylinders.

B. Detrending strategy: axial trend removal and weak-stationary residual

Having defined the burrowsity field and identified the dominant sources of nonstationarity (beam hardening/cupping, ring artifacts, and slow axial drift), the detrending operator used to produce an analysis field suitable for second-order (covariance/spectral) convergence tests is specified in this subsection.

Because the acquisition domain is a finite cylinder aligned with the z axis, a natural and conservative first step is the removal of trends that manifest as slow variations of the slice-wise phase fraction along z . In what follows, it is assumed that the axial profile $\phi(z_k)$ and the moving-average trend $\mu_w(z_k)$ have already been defined in Eqs. (4) and (5), and that the voxel-level detrended field $b(\mathbf{x})$ has been defined in Eq. (6).

The centered moving-average trend in Eq. (5) is applied *only* to the slice-wise axial profile $\phi(z_k)$, i.e., to the one-dimensional discrete sequence $\phi_k \equiv \phi(z_k)$ indexed by the slice number k (with spacing Δz). Accordingly,

the associated transfer function is a *one-dimensional axial* frequency response. Denoting by ω_z the discrete axial angular frequency (in rad/slice; equivalently $\kappa_z = \omega_z/\Delta z$ in rad/mm), the moving-average kernel of width w has transfer function

$$H_w(\omega_z) = \frac{1}{w} \frac{\sin(\frac{w\omega_z}{2})}{\sin(\frac{\omega_z}{2})} e^{-i\omega_z(w-1)/2}, \quad (11)$$

so that higher- ω_z content in the *axial* profile is systematically suppressed as w is increased, while the lowest- ω_z drift is retained in the trend estimate. This interpretation is useful for REV sizing because the subsequent \widehat{C} -test is explicitly sensitive to low-wavenumber structure: any residual drift leaking into b inflates apparent correlation scales and biases diameter selection toward overly large values.

In the present workflow, the primary tuning diagnostic is the residual excess kurtosis $K_{\text{ex}}(w)$ defined in Eq. (9). To complement this distributional diagnostic with a second-order criterion aligned with the later covariance analysis, the normalized autocovariance of the axial residual may also be monitored,

$$\begin{aligned} \tilde{R}_r(\ell; w) = & \frac{1}{(M-\ell)\sigma_r^2(w)} \\ & \sum_{k=1}^{M-\ell} (r(z_k; w) - \bar{r}(w))(r(z_{k+\ell}; w) - \bar{r}(w)), \end{aligned} \quad (12)$$

where $\sigma_r^2(w)$ is the sample variance of $r(\cdot; w)$. A compact window-selection score may then be defined as

$$S(w) = \sum_{\ell=1}^{\ell_{\text{max}}} \left| \tilde{R}_r(\ell; w) \right|, \quad (13)$$

with ℓ_{max} chosen as a small fraction of M (e.g., $\ell_{\text{max}} \sim 0.1M$). In practice, a regime is sought in which both $K_{\text{ex}}(w)$ and $S(w)$ vary weakly with further increases of w , indicating that axial drift has been removed without artificially erasing intermittent burrow-driven variability.

Axial detrending addresses drift in $\phi(z_k)$ but does not, by itself, remove structured in-slice artifacts. If rings are present, spurious radial correlation can be introduced that directly contaminates the radial covariance and spectrum used later. Therefore, when ring structure is evident by inspection or by strong narrowband peaks in the 2D Fourier domain of slices, ring-reduction should be performed prior to computing C and \widehat{C} [18, 19]. Similarly, strong beam-hardening/cupping gradients should be corrected during reconstruction or normalized post hoc to avoid biasing large-scale statistics [17, 22].

All subsequent diameter tests are formulated in terms of second-order statistics (covariance and spectral descriptors). Accordingly, the operational objective of the present preprocessing is that the detrended field b exhibits an approximately constant mean over the analysis

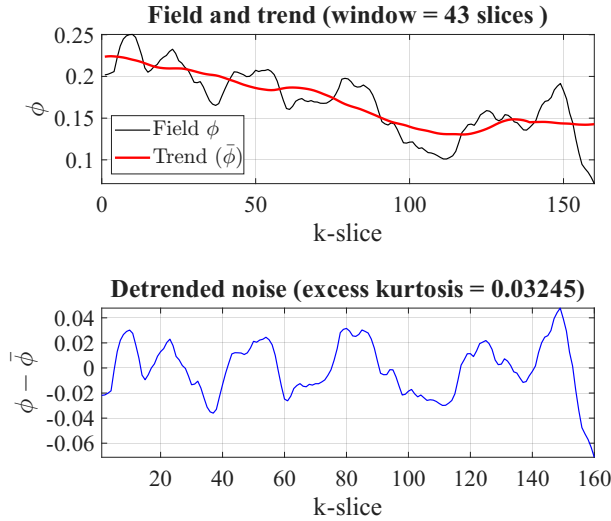


FIG. 2. Axial detrending of the slice-wise phase-fraction signal. Top: slice-wise phase fraction $\phi(z_k)$ (black) and the corresponding moving-average trend $\bar{\phi}(z_k)$ (red) computed with window width w (in slices). Bottom: residual $r(z_k) = \phi(z_k) - \bar{\phi}(z_k)$ (blue), used to quantify how much low-frequency drift remains after detrending and to guide the choice of w via residual diagnostics (e.g., excess kurtosis).

window and that its covariance is governed primarily by spatial separation (weak stationarity within estimation uncertainty). The \hat{C} -based diameter convergence test in the next section is computed exclusively on b .

Equations (4), (5), (6), and (9) define (i) the axial phase-fraction profile, (ii) a smooth trend obtained by a moving-average window of width w , (iii) the voxel-level detrended field, and (iv) residual diagnostics used to select w . Figure 2 illustrates the decomposition for a representative choice of w , while Fig. 3 summarizes the window sweep used to identify a robust trend/noise separation scale. Through this selection, the axial extent over which the residual field can be treated as approximately weakly stationary for the second-order analysis performed below is fixed.

III. \hat{C} -TEST FOR OPTIMAL DIAMETER

Through the preprocessing described in Sec. II, a detrended residual field $b(\mathbf{x})$ [Eq. (6)] is obtained in which slow drift and structured acquisition artifacts have been reduced to the extent required for second-order analysis. In the present section, a geometric and statistical objective is pursued: for a finite CT cylinder, the smallest diameter is determined for which second-order descriptors of b are stable within a prescribed tolerance.

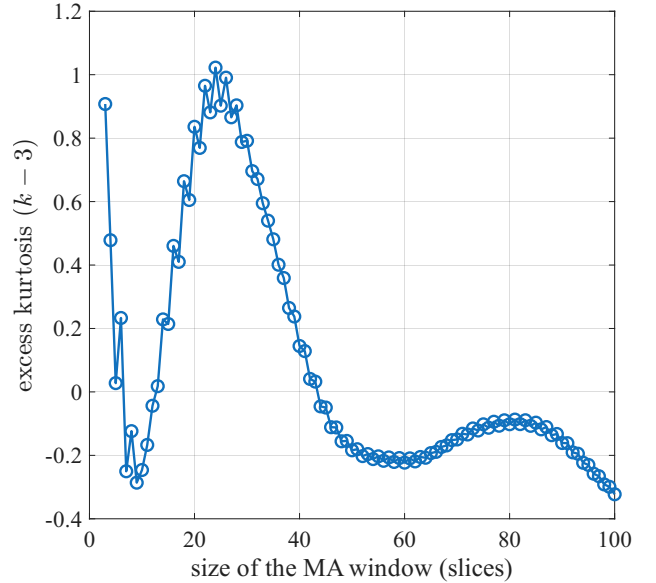


FIG. 3. Excess kurtosis $K_{\text{ex}}(w)$ of the detrended axial residual as a function of the moving-average window width w . Because a Gaussian residual has $K_{\text{ex}} = 0$, zero-crossings of $K_{\text{ex}}(w)$ are used as a practical criterion for selecting a detrending scale. Among the candidate windows where $K_{\text{ex}}(w) \approx 0$, the largest window is chosen to suppress slow axial drift most strongly while maintaining a residual that is approximately Gaussian.

A. From disk averages to a spectral stability criterion

As an empirical proxy for representativeness, the stabilization of spatial averages under increasing window size is often employed. On a cross section at $z = z_k$ (or on a short axial window centered on z_k), the slice-restricted residual is introduced as

$$b_k(\mathbf{x}_\perp) = b(\mathbf{x}_\perp, z_k), \quad \mathbf{x}_\perp = (x, y), \quad (14)$$

and is defined on the in-slice disk $\|\mathbf{x}_\perp\| \leq R$ imposed by the cylindrical mask. The concentric disk average of b_k over radius r is then given by

$$\langle b_k \rangle(r) = \frac{1}{\pi r^2} \int_{\|\mathbf{x}_\perp\| \leq r} b_k(\mathbf{x}_\perp) d\mathbf{x}_\perp, \quad 0 < r \leq R. \quad (15)$$

For small r , $\langle b_k \rangle(r)$ is dominated by individual burrow segments and junctions. As r is increased, disk averaging is effectively applied as a low-pass filter, and progressively higher spatial frequencies are attenuated.

In the spectral domain, this filtering interpretation is made explicit. Under the working assumption that b_k may be treated as approximately weakly stationary *within the transverse cross section* at fixed $z = z_k$, the variance of the disk average can be expressed as a weighted integral of the *isotropic transverse* power spectrum $\hat{C}_\perp(k_\perp)$ associated with the two-point covariance

of b_k ,

$$\text{Var}[\langle b_k \rangle(r)] = \frac{1}{2\pi} \int_0^\infty \hat{C}_\perp(k_\perp) |W_r(k_\perp)|^2 k_\perp dk_\perp, \quad (16)$$

where $k_\perp = \|\mathbf{k}_\perp\|$ denotes the radial wavenumber in the (x, y) plane and $W_r(k_\perp)$ is the transfer function of the normalized circular window used in Eq. (15). For a normalized radius- r disk in 2D,

$$W_r(k_\perp) = \frac{2J_1(k_\perp r)}{k_\perp r}, \quad (17)$$

with J_1 denoting the Bessel function of the first kind. The distinction from the axial detrending filter should be stressed: $H_w(\omega_z)$ [Eq. (11)] is a *one-dimensional* transfer function acting on the axial (z -direction) profile $\phi(z_k)$, whereas $W_r(k_\perp)$ is a *two-dimensional transverse* transfer function acting on in-plane (x, y) fluctuations within each slice. Equations (16)–(17) formalize the practical point that the stabilization of disk-averaged observables is controlled by the low- k (long-wavelength) content of $\hat{C}(k)$. On this basis, a diameter criterion is naturally motivated in which convergence is tested directly on $\hat{C}(k)$, rather than on any particular choice of averaged observable.

B. Operational definition of the \hat{C} -test on nested cylinders

Let $\Omega(D)$ denote the concentric inscribed cylinder of diameter D extracted from the full scan, with a fixed axis and an axial window selected using w^* as described in Sec. II. For each D , an isotropized in-slice covariance $C_D(r)$ of the residual fluctuations is computed, and its isotropic spectrum $\hat{C}_D(k)$ is obtained via the 2D Hankel transform

$$\hat{C}_D(k) = 2\pi \int_0^\infty C_D(r) r J_0(kr) dr, \quad (18)$$

where J_0 is the Bessel function of the first kind. A diameter is declared representative once the low-wavenumber part of $\hat{C}_D(k)$ is found to be insensitive to further increases of D .

To make the criterion explicit and reproducible, a convergence metric is evaluated over a prescribed low- k interval $[0, k_c]$:

$$\varepsilon(D_m) = \frac{\left(\int_0^{k_c} [\hat{C}_{D_m}(k) - \hat{C}_{D_{m-1}}(k)]^2 dk \right)^{1/2}}{\left(\int_0^{k_c} \hat{C}_{D_{m-1}}(k)^2 dk \right)^{1/2}}, \quad (19)$$

and the smallest D_m is selected such that $\varepsilon(D_m) \leq \tau$, where τ is a user-set tolerance. The cutoff k_c is chosen to probe wavelengths comparable to, and larger than, the dominant burrow-network connectivity scale, since that regime is typically responsible for the strongest diameter dependence in burrowed fabrics.

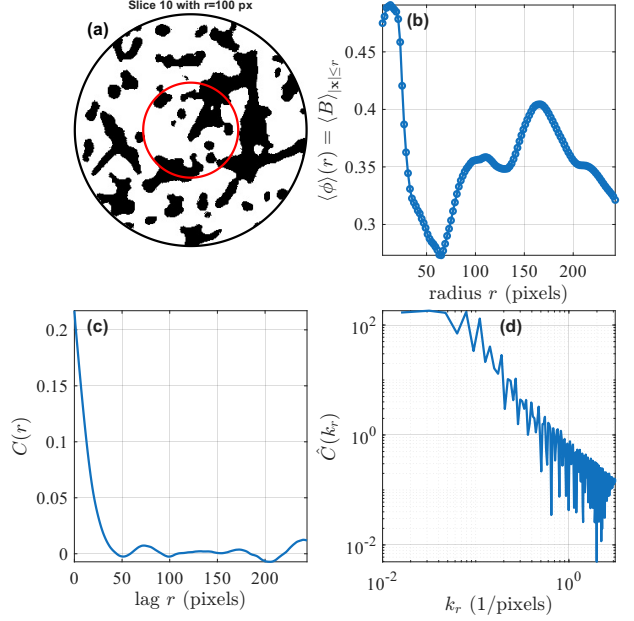


FIG. 4. Slice-wise statistics for a *Thalassinoides* core. (a) Boolean slice B_{slice} (burrow/phase pixels in black, background in white) with a concentric sampling circumference of radius r overlaid in red. (b) Enclosed area fraction $\langle \phi \rangle(r) = \langle B_{\text{slice}} \rangle_{|\mathbf{x}| \leq r}$ as a function of radius. (c) Two-point covariance $C(r)$ computed on the slice within an inscribed circular region. (d) Radial spectrum $\hat{C}(k_r)$ obtained from $C(r)$ using the 2D isotropic Hankel transform.

C. Slice-wise diagnostics and interpretation

In Fig. 4, complementary readouts are summarized as they are used in practice on a representative cross section extracted from $\Omega(D)$. In panel (a), a Boolean slice (after masking) is shown together with the concentric disk used for the average in Eq. (15). In panel (b), the corresponding enclosed-area fraction (disk-average proxy) is reported as a function of r . In panels (c) and (d), the second-order descriptors used in the \hat{C} -test are provided: the isotropic covariance $C_D(r)$ and its isotropic spectrum $\hat{C}_D(k)$ obtained from Eq. (18). In the spectral representation, a transition to a low- k plateau is interpreted as evidence that the largest resolved wavelengths are being sampled consistently; stability of that low- k content under increasing D is precisely the condition enforced by Eq. (19). For reporting purposes, a characteristic scale may additionally be extracted from the onset k_0 of the plateau and converted to a radius through $r_{\text{REV}} \sim \alpha/k_0$; the explicit convergence test above provides the reproducible criterion, while the plateau-based scale serves as an interpretable diagnostic.

IV. NUMERICAL RESULTS

In this section, the preprocessing protocol described in Sec. II and the \widehat{C} -based diameter criterion introduced in Sec. III are applied to the segmented *Thalassinoides* μ CT cylinder shown in Fig. 1. Two objectives are pursued: (i) dimensionless outputs of the detrending and spectral procedures (window size in slices, plateau wavenumber in pixels^{-1}) are converted into physical REV dimensions, and (ii) the resulting dimensions are interpreted as practical guidelines for subvolume extraction and subsequent digital-rock calculations.

A. Voxel spacing and geometric calibration

The reconstructed volume is defined on a grid of size $N_x \times N_y \times N_z = 488 \times 488 \times 160$ voxels and corresponds to a physical specimen of diameter $D_s = 180$ mm and height $H_s = 310$ mm (Fig. 1). Under the standard linear mapping between pixel counts and specimen dimensions, the voxel spacings are

$$\Delta x = \Delta y = \frac{D_s}{N_x} \simeq \frac{180}{488} \approx 0.369 \text{ mm/pixel},$$

$$\Delta z = \frac{H_s}{N_z} \simeq \frac{310}{160} \approx 1.94 \text{ mm/slice}.$$

Anisotropic resolution is therefore present ($\Delta z \gg \Delta x$), as is typical when full-height scanning is combined with limited axial sampling. This anisotropy motivates the two-stage sizing logic developed above: the axial extent is determined by an axial stationarity criterion (Sec. II), whereas the transverse diameter is determined by a radial/spectral criterion evaluated on slices (Sec. III).

B. Axial REV height from detrending window selection

The axial detrending analysis is performed on the slice-wise phase-fraction signal, and a moving-average window width w (in slices) is selected such that slow drift is removed while intermittent fluctuations associated with burrow-network heterogeneity are retained. The window sweep summarized in Fig. 3 yields multiple candidate roots/plateau regimes; following the conservative choice specified in Sec. II, the largest robust window, $w^* = 43$ slices, is selected. The corresponding axial length scale is

$$H_{\text{REV}} = w^* \Delta z \approx 43 \times 1.94 \text{ mm} \approx 83.3 \text{ mm}.$$

Operationally, H_{REV} is interpreted as the minimum axial extent over which the detrended burrowsity residual can be treated as approximately weakly stationary

for the subsequent second-order analysis. In practice, the \widehat{C} -test (and any later property estimation performed on extracted cylinders) should be restricted to axial windows of length at least H_{REV} . A principled definition of the axial window used when comparing nested diameters is also provided: diameter dependence is to be assessed at fixed axial extent so that axial drift effects are not conflated with transverse finite-size effects.

C. Transverse REV radius from the low- k plateau

A \widehat{C} -based criterion was applied so that the long-wavelength content of the microstructure sampled within a disk cross section was targeted (Sec. III). In the present dataset, a transition to a low- k plateau was observed in the radial spectrum (Fig. 4), and the onset of this plateau was identified at approximately

$$k_0 \simeq 0.05 \text{ pixel}^{-1}.$$

This onset was interpreted as the wavenumber associated with the dominant connectivity scale controlling diameter dependence, and an REV radius in pixel units was estimated as

$$r_{\text{REV}} \approx \frac{2\pi}{k_0} \approx \frac{2\pi}{0.05} \approx 125.7 \text{ pixels}.$$

Conversion to physical units was then carried out using Δx (Sec. IV), giving

$$r_{\text{REV}} \approx 125.7 \Delta x \approx 125.7 \times 0.369 \text{ mm} \approx 46.3 \text{ mm},$$

and hence

$$D_{\text{REV}} = 2r_{\text{REV}} \approx 92.7 \text{ mm}.$$

Two points were emphasized.

First, the inferred D_{REV} was found to be a substantial fraction of the specimen diameter,

$$\frac{D_{\text{REV}}}{D_s} \approx \frac{92.7}{180} \approx 0.52,$$

which was consistent with the qualitative challenge posed by *Thalassinoides* fabrics: when a connected burrow network exhibits centimeter-scale connectivity, a standard core diameter can sample only a limited number of the longest-wavelength features, and representativeness in the transverse direction is then governed by a small set of dominant structures.

Second, the radius estimate was interpreted as a statistically motivated *minimum* diameter for stable second-order descriptors of the detrended field. For diameters below D_{REV} , the low-wavenumber content was undersampled, and the inferred correlation structure (and any downstream connectivity-driven property proxy) remained diameter-dependent. For diameters above D_{REV} , progressively less new low- k information was added as the cylinder was enlarged, and the covariance/spectrum descriptors were thus expected to stabilize within the prescribed tolerance.

D. Combined REV estimate and practical implications

Taken together, the axial window selected by the detrending procedure (Sec. II) and the transverse diameter selected by the \widehat{C} -stability criterion (Sec. III) defined a practical REV-sized extraction cylinder for the present sample, with $D_{\text{REV}} \approx 93$ mm and $H_{\text{REV}} \approx 83$ mm. These values were interpreted as the smallest cylinder dimensions for which reproducible second-order structure (covariance and low- k spectral content) was obtained for the detrended burrowsity field under further enlargement of the domain. In this sense, D_{REV} provided a defensible minimum field of view for downstream digital-rock analyses controlled by long-wavelength connectivity, including correlation-length reporting and the construction of simulation domains in which a small number of connected burrow junctions could otherwise bias effective-property estimates.

Finally, the scope of the estimate was kept explicit. The reported values followed from (i) the detrending window selection rule used to define w^* and (ii) the plateau identification used to determine k_0 . Both steps were transparent and reproducible (Figs. 2–4), but threshold sensitivity remained. For practical reporting, it was therefore recommended that the selected w^* and the identified k_0 be documented alongside the final physical REV dimensions, and that modest variations of these intermediate quantities be treated as an uncertainty band on D_{REV} and H_{REV} rather than as a contradiction of the method.

V. CONCLUSIONS

In *Thalassinoides*-bearing rocks, pore-scale variability is combined with a strongly connected, centimeter-scale burrow architecture, so that the stability of image-derived descriptors can be dominated by finite-size effects at wavelengths comparable to the scanned diameter. In the present work, this issue was addressed by casting REV sizing as a *second-order convergence* problem on a finite CT cylinder. A reproducible burrowsity field was

defined, and an explicit detrending/denoising step was applied so that slow drift and structured CT artifacts were suppressed. The resulting residual field was then used as input to a diameter-selection test in which representativeness was enforced through the convergence of the low-wavenumber content of \widehat{C} on nested cylinders.

When the protocol was applied to the present dataset, an REV-consistent axial extent of approximately $H_{\text{REV}} \approx 83$ mm was obtained from the axial detrending of the slice-wise phase-fraction signal, while an REV-scale diameter of $D_{\text{REV}} \approx 93$ mm was indicated by the \widehat{C} -based stability criterion. When interpreted jointly, these values were taken to define a recommended *minimum* cylindrical analysis domain for correlation-descriptor reporting and for downstream digital-rock workflows in which long-wavelength connectivity exerts dominant control.

Beyond the present specimen, the main outcome was methodological: by linking REV sizing to the convergence of covariance/spectral descriptors—rather than to a particular averaged observable—the mechanism responsible for diameter dependence in connectivity-dominated media was targeted directly. In future work, the diameters selected by \widehat{C} will be benchmarked against the convergence of transport and mechanical observables (e.g., directional permeability proxies or elastic responses), and sensitivity to segmentation choices and residual artifact levels will be quantified.

VI. DATA AVAILABILITY

MATLAB script used to generate the numerical results and figures in this work, together with example input and output data, are openly available in the GitHub repository https://github.com/quantumfi/REV_sizing.

ACKNOWLEDGMENTS

We thank Khalid Abdelbasit and Hassan Eltom for their help with fieldwork, and Hani Salman Al Mukainah at KFUPM for assisting with the CT-scan acquisition.

[1] D. Knaust, *The trace fossil thalassinoides paradoxicus kennedy, 1967 revisited from its type locality (albian–cenomanian chalk, se england)*, Palaeogeography, Palaeoclimatology, Palaeoecology **634**, 111913 (2024).

[2] H. A. Eltom and A. M. Alqubalee, *Quantitative variability of burrow percentage estimated from 2d views: Example from thalassinoides-bearing strata, central saudi arabia*, PALAIOS **37**, 35–43 (2022).

[3] H. A. Eltom, A. Alqubalee, and M. A. Yassin, *Potential overlooked bioturbated reservoir zones in the shallow marine strata of the hanifa formation in central saudi arabia*, Marine and Petroleum Geology **124**, 104798 (2021).

[4] A. A. Ekdale and R. G. Bromley, *Paleoethologic interpretation of complex thalassinoides in shallow-marine limestones, lower ordovician, southern sweden*, Palaeogeography, Palaeoclimatology, Palaeoecology **192**, 221–227 (2003).

[5] R. G. Bromley and R. W. Frey, *Redescription of the trace fossil gyrolithes and taxonomic evaluation of thalassinoides, ophiomorpha and spongeliomorpha*, Bulletin of the Geological Society of Denmark **23**, 311–335 (1974), legacy article; DOI not assigned.

[6] H. A. Eltom, A. M. Alqubalee, A. S. Sultan, A. A. Barri, and K. Abdelbasit, *Understanding the permeability of*

burrow-related gas reservoirs through integrated laboratory techniques, Journal of Natural Gas Science and Engineering **90**, 103917 (2021).

[7] H. A. Eltom and R. H. Goldstein, *Use of geostatistical modeling to improve understanding of permeability upscaling in isotropic and anisotropic burrowed reservoirs*, Marine and Petroleum Geology **129**, 105067 (2021).

[8] H. Andrä, N. Combaret, J. Dvorkin, E. Glatt, J. Han, M. Kabel, Y. Keehm, F. Krzikalla, M. Lee, C. Madonna, M. Marsh, T. Mukerji, E. H. Saenger, R. Sain, N. Saxena, S. Ricker, A. Wiegmann, and X. Zhan, *Digital rock physics benchmarks—part II: Computing effective properties*, Computers & Geosciences **50**, 33–43 (2013).

[9] T. Bultreys, W. De Boever, and V. Cnudde, *Imaging and image-based fluid transport modeling at the pore scale: A review*, Earth-Science Reviews **155**, 93–128 (2016).

[10] J. Bear, *Dynamics of Fluids in Porous Media* (American Elsevier Publishing Company, New York, 1972).

[11] M. Ostoja-Starzewski, *Material spatial randomness: From statistical to representative volume element*, Probabilistic Engineering Mechanics **21**, 112–132 (2006).

[12] T. Kanit, S. Forest, I. Galliet, V. Mounoury, and D. Jeulin, *Determination of the size of the representative volume element for random composites: Statistical and numerical approach*, International Journal of Solids and Structures **40**, 3647–3679 (2003).

[13] S. Torquato, *Random Heterogeneous Materials: Microstructure and Macroscopic Properties* (Springer, New York, 2002).

[14] R. Al-Raoush and A. Papadopoulos, *Representative elementary volume analysis of porous media using X-ray computed tomography*, Powder Technology **200**, 69–77 (2010).

[15] S. Schlüter, A. P. Sheppard, K. Brown, and D. Wildenschild, *Image processing of multiphase images obtained via X-ray microtomography: A review*, Water Resources Research **50**, 3615–3639 (2014).

[16] C. Tantardini and F. Alonso-Marroquin, *Capillarity in stationary random granular media: Distribution-aware screening and quantitative supercell sizing* (2025), arXiv:2509.21350 (v2, revised 8 Dec 2025), arXiv:2509.21350 [cond-mat.soft].

[17] R. A. Brooks and G. Di Chiro, *Beam hardening in x-ray reconstructive tomography*, Radiology **118**, 373–377 (1976).

[18] J. F. Barrett and N. Keat, *Artifacts in CT: Recognition and avoidance*, Radiographics **24**, 1679–1691 (2004).

[19] J. Sijbers and A. Postnov, *Reduction of ring artefacts in high resolution micro-CT reconstructions*, Physics in Medicine and Biology **49**, N247–N253 (2004).

[20] N. Otsu, *A threshold selection method from gray-level histograms*, IEEE Transactions on Systems, Man, and Cybernetics **9**, 62–66 (1979).

[21] P. Iassonov, T. Gebrenegus, and M. Tuller, *Segmentation of x-ray computed tomography images of porous materials: A crucial step for characterization and quantitative analysis of pore structures*, Water Resources Research **45**, W09415 (2009).

[22] R. A. Ketcham and R. D. Hanna, *Beam hardening correction for x-ray computed tomography of heterogeneous natural materials*, Computers & Geosciences **67**, 49–61 (2014).

[23] D. Wildenschild and A. P. Sheppard, *X-ray imaging and analysis techniques for quantifying pore-scale structure and processes in subsurface porous medium systems*, Advances in Water Resources **51**, 217–246 (2013).

[24] A. Singh, K. Regenauer-Lieb, S. D. C. Walsh, R. T. Armstrong, J. J. M. van Griethuysen, and P. Mostaghimi, *On representative elementary volumes of grayscale micro-ct images of porous media*, Geophysical Research Letters **47**, e2020GL088594 (2020).

[25] K. Arias-Calluari, M. N. Najafi, M. S. Harré, Y. Tang, and F. Alonso-Marroquin, *Testing stationarity of the detrended price return in stock markets*, Physica A: Statistical Mechanics and its Applications **587**, 126487 (2022).